Construction of EuF_3 hollow sub-microspheres and single-crystal hexagonal microdiscs *via* Ostwald ripening and oriented attachment

Zhiming Chen,[a] Zhirong Geng,[a] Menglu Shi,[a] Zhihui Liu[b] and Zhilin Wang*[a]

Received 11th February 2009, Accepted 24th March 2009
First published as an Advance Article on the web 7th April 2009
DOI: 10.1039/b902838b

Hexagonal phase EuF_3 hollow sub-microspheres and single-crystal hexagonal microdiscs with controllable sizes were fabricated *via* a facile hydrothermal route at 110 °C for 8 and 14 h, respectively. Increasing the $Eu(NO_3)_3$ concentration (from 0.125 to 0.2 M) increased the size of the microdiscs, but decreased the diameter of the sub-microspheres. Detailed investigations on samples at different preparation stages revealed that the hollow sub-microspheres were formed *via* a self-transformation process within the same aggregated particles accompanied by the localized Ostwald ripening. Subsequently, hexagonal microdiscs were achieved at the consumption of the hollow sub-microspheres, which were attributed to oriented attachment mechanism. Moreover, the Ostwald ripening mechanism acted to form the secondary particles before the attachment. This kind of cooperation of two basic mechanisms may give us a new insight into the growth of EuF_3 microcrystals and opens a new way for controllable synthesis of other well-defined crystals in morphology and dimensionality.

Introduction

The past few years have witnessed significant advances in the synthesis of nano- and micromaterials with well-defined and controllable morphologies, because it is well known that the properties of the materials closely interrelate with geometrical factors such as morphology, dimensionality, and size.[1–4] Traditional solution—synthetic methods, especially the hydrothermal processes, have been widely used for the controlled synthesis of various nano- and micromaterials. There are two basic crystal growth mechanisms in solution systems. The first one, known as Ostwald ripening, has been proven to be a facile approach for generating symmetric and asymmetric interior spaces, including core-shell spaces and multiple shell spaces, for inorganic nanostructures,[5–17] which involved the growth of larger particles at the expense of smaller ones. According to the Gibbs–Thompson equation[18] and Fick's first law, the chemical potential of a particle increases with a decrease in particle size, which means that the equilibrium solute concentration near a small particle is higher than that near a larger one. The resulting concentration gradients would lead to the diffusion of molecular-scale species from smaller particles to larger particles through solution. The second one, pictured today as oriented attachment, has been described as a versatile approach for construction of nanomaterials, which related to the direct self-organization of two particles into a single crystal by sharing a common crystallographic orientation, despite the presence of strong surface-bound ligands.[19,20] Up to now, several kinds of oriented aggregation and the relationships among zero-, one-, two-, and three-dimensional (0D, 1D, 2D and 3D) materials in the structural transformations have been elucidated.[21] However, owing to the complexity of the influencing factors, the controlled synthesis in morphology and dimensionality has still been a tremendous challenge for scientists.

Rare-earth fluorides with controllable shapes and sizes attracted considerable attention as they are widely used in luminescence, biochemical probes, and medical diagnostics for their unique luminescence properties.[22–25] The luminescence of rare-earth ions mainly arises from the 4f electrons, which is highly sensitive to the composition and structure of the host materials. Fluorides have an advantage as a fluorescent host matrix owing to their low vibrational energies,[26] and the subsequent minimization of the quenching of the rare-earth-ion excited states, yielding high quantum efficiency. By now, different morphologies of binary rare-earth fluoride crystals based on different solution-based routes have been prepared, including fullerene-like lanthanide fluorides,[27,28] bundle-like and rod-like YF_3,[26,29] hexagonal and triangular YF_3 nanocrystals,[30] polyhedral YF_3 microcrystals,[31] PrF_3 hollow nanoparticles,[32] monodispersed LaF_3 triangular nanoplates,[33] EuF_3 nanoflower,[34] and EuF_3 nanocrystals with different morphologies.[35,36] However, to the best of our knowledge, the synthesis of EuF_3 hollow sub-microspheres and hexagonal microdisc crystals has not yet been reported in literatures. Accordingly, the fabrication of EuF_3 hollow sub-microspheres and hexagonal microdisc crystals, and investigation of their formations was carried out.

In the present work, we reported a simple synthetic scheme for preparation of EuF_3 hollow sub-microspheres and hexagonal microdisc crystals. The morphology transformations of these structures were investigated systematically. A crystal growth approach was demonstrated to address the formation of EuF_3 spherical structures and hexagonal microdisc crystals. In the process of the formation, solid EuF_3 spheres were formed by a self-assembly of primary colloidal particles and then gradually developed into sub-microspheres with hollow interiors due to the

[a]*State Key Laboratory of Coordination Chemistry, School of Chemistry and Chemical Engineering, Nanjing University, Nanjing, 210093, People's Republic of China. E-mail: wangzl@nju.edu.cn; Fax: +86-25-83317761; Tel: +86-25-83686082*
[b]*School of Life Science, Nanjing University, Nanjing, 210093, People's Republic of China*

localized Ostwald ripening mechanism, while the hexagonal microdisc crystals were formed *via* an oriented attachment mechanism.

Results and discussion

EuF_3 hollow sub-microspheres were prepared by hydrothermal treatment of the mixed system at 110 °C for 8 h (see Experimental section). Fig. 1a and 1b show transmission electron microscopy (TEM) images of the product obtained in 0.2 M $Eu(NO_3)_3$ solution at 110 °C for 8 h and reveal that the sample is in the form of hollow sub-microspheres with a diameter of 250–320 nm. The corresponding selected area electron diffraction (SAED) pattern in Fig. 1c indicates that the EuF_3 hollow microspheres are polycrystalline and the most distinct four concentric diffraction rings can be indexed to (302), (222), (404) and (332) planes from the center, sequentially. The high-resolution transmission electron microscopy (HRTEM) image of a single sub-microsphere (Fig. 1d), indicating that the distance between the adjacent lattice planes is 0.313 nm, is ascribed to (111) crystal planes of the hexagonal phase EuF_3.

EuF_3 hexagonal microdisc crystals were fabricated by extending the heating time to 14 h. Fig. 2a and 2b display typical scanning electron microscopy (SEM) and TEM images of the sample obtained in 0.2 M $Eu(NO_3)_3$ solution at 110 °C for 14 h, indicate that the product is hexagonal microdiscs with a diameter of about 1.1–1.2 μm. The regular hexagonal cross-sections can be observed easily (Fig. 2b), and correspond to hexagonal microdiscs standing on the bottom face parallel to the substrate. The corresponding SAED pattern was recorded by focusing the electron beam on one of the hexagonal facets of the microdisc crystal, which shows that the as-prepared EuF_3 microdisc crystal is single-crystalline. The inner set of spots can be indexed to

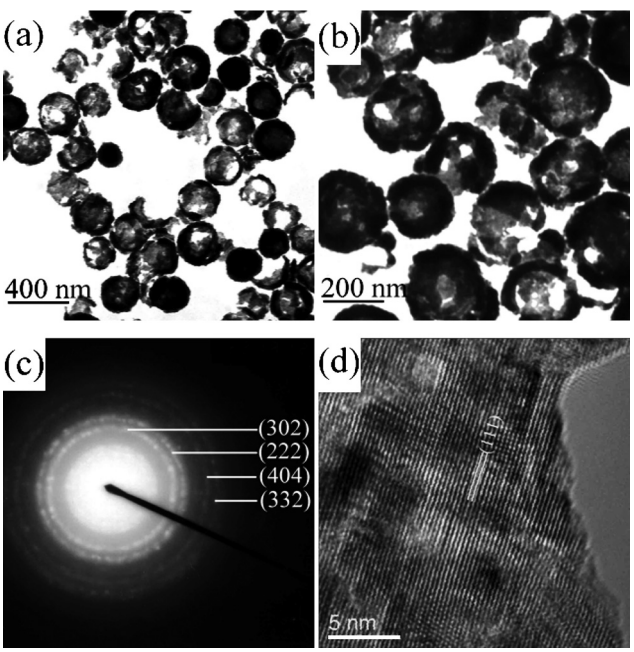

Fig. 1 (a) and (b) TEM images of EuF_3 hollow sub-microspheres obtained in 0.2 M $Eu(NO_3)_3$ solution at 110 °C for 8 h; (c) SAED and (d) HRTEM images of EuF_3 hollow sub-microspheres, respectively.

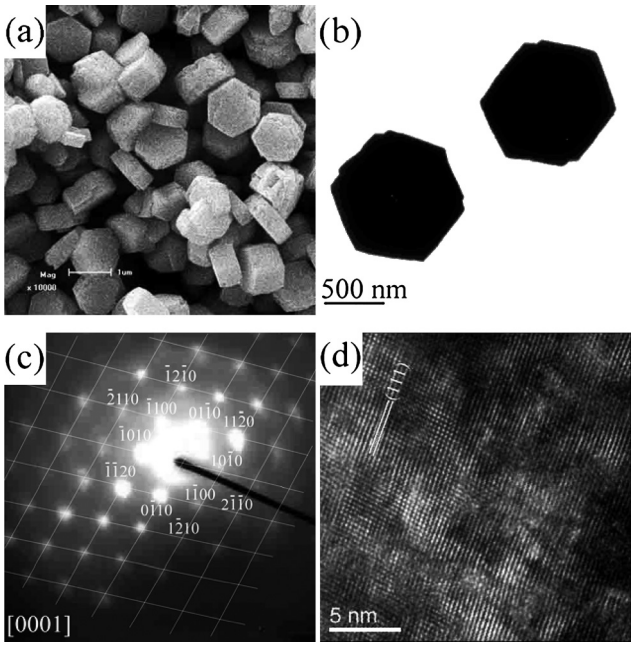

Fig. 2 (a) SEM and (b) TEM images of EuF_3 hexagonal microdisc crystals obtained in 0.2 M $Eu(NO_3)_3$ solution at 110 °C for 14 h; (c) SAED and (d) HRTEM images of the hexagonal microdisc crystals, respectively.

[0001] zone of hexagonal EuF_3 (Fig. 2c). Fig. 2d shows a well-crystallized structure with lattice fringes of *ca* 0.311 nm, corresponding to the (111) lattice planes of hexagonal EuF_3.

The composition and phase purity of the products were examined by powder X-ray diffraction (XRD). Fig. 3a and 3b show the XRD patterns of typical EuF_3 hollow sub-microspheres and hexagonal microdisc crystals obtained in 0.2 M $Eu(NO_3)_3$ solution at 110 °C for 8 and 14 h, respectively. All diffraction peaks of the hollow sub-microspheres and hexagonal microdiscs can be readily indexed to hexagonal phase of EuF_3 with lattice

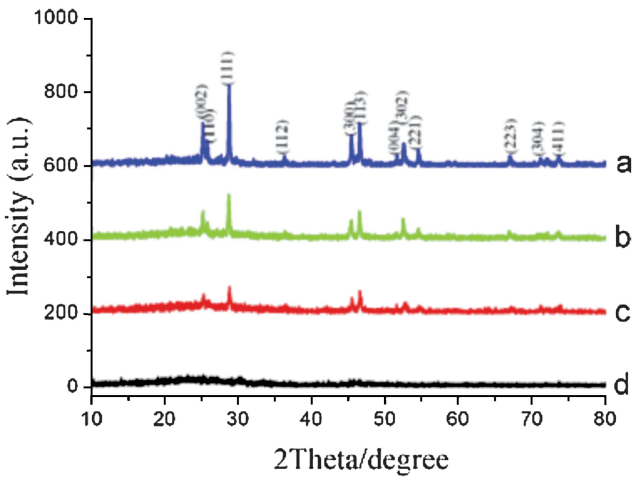

Fig. 3 XRD patterns for (a) EuF_3 hexagonal microdisc crystals, (b) EuF_3 hollow sub-microspheres, (c) EuF_3 spherical aggregates, and (d) EuF_3 primary particles, which were obtained in 0.2 M $Eu(NO_3)_3$ solution at 110 °C for (a) 14 h, (b) 8 h, (c) 6 h, and (d) without hydrothermal treatment, respectively.

constants $a = 6.920$ Å and $c = 7.085$ Å (JCPDS 32-0373). It is worth pointing out that the XRD patterns indicate a progressive increase in the crystallinity of the microdisc crystals.

The hollow sub-microspheres with a smaller or larger diameter could be easily fabricated by increasing or decreasing the concentration of $Eu(NO_3)_3$, respectively (Table 1). As 8 ml of 0.125 M $Eu(NO_3)_3$ solution was used, most products were sub-microspheres with a diameter of *ca* 410–450 nm (Fig. 4a). When 7.5 ml of 0.133 M $Eu(NO_3)_3$ solution was employed, EuF_3 sub-microspheres with a diameter of *ca* 410–450 nm were prepared (Fig. 4b). Increasing the concentration of $Eu(NO_3)_3$ to 0.143 M, a plenty of uniform and regular sub-microspheres with a diameter of *ca* 300–330 nm were obtained. Simultaneously, some broken spheres could also be observed (Fig. 4c). With further increasing the concentration of $Eu(NO_3)_3$ to 0.154 M, the size of the obtained sub-microspheres decreases to 280–320 nm (Fig. 4d). It was also found that the size of EuF_3 hexagonal microdisc crystals can be controlled by adjusting the concentration of $Eu(NO_3)_3$ (Table 1). Prolonging the hydrothermal time to 14 h, EuF_3 hexagonal microdisc crystals with diameters of *ca* 1.1–1.25 μm, 0.7–1.0 μm, 0.5–0.85 μm and 0.4–0.55 μm were formed in 0.200, 0.182, 0.154, and 0.143 M $Eu(NO_3)_3$ solution, respectively. The SEM images show that these hexagonal microdisc crystals had a low aspect ratio (Fig. 5), suggesting a low anisotropic growth of the microcrystals.

Table 1 Effect of $Eu(NO_3)_3$ concentration and hydrothermal time on the products

Additive water/ml	$Eu(NO_3)_3$ solution				
	V/ml	*C*/M	*t*/h	Morphology	Diameter/nm
0	5	0.200	8	hollow sub-microspheres	250–320
1.5	6.5	0.154	8	hollow sub-microspheres	280–320
2	7	0.143	8	hollow sub-microspheres	300–330
2.5	7.5	0.133	8	hollow sub-microspheres	350–400
3	8	0.125	8	hollow sub-microspheres	410–450
0	5	0.200	14	hexagonal microdiscs	1100–1250
0.5	5.5	0.182	14	hexagonal microdiscs	700–1000
1.5	6.5	0.154	14	hexagonal microdiscs	500–850
2	7	0.143	14	hexagonal microdiscs	400–550

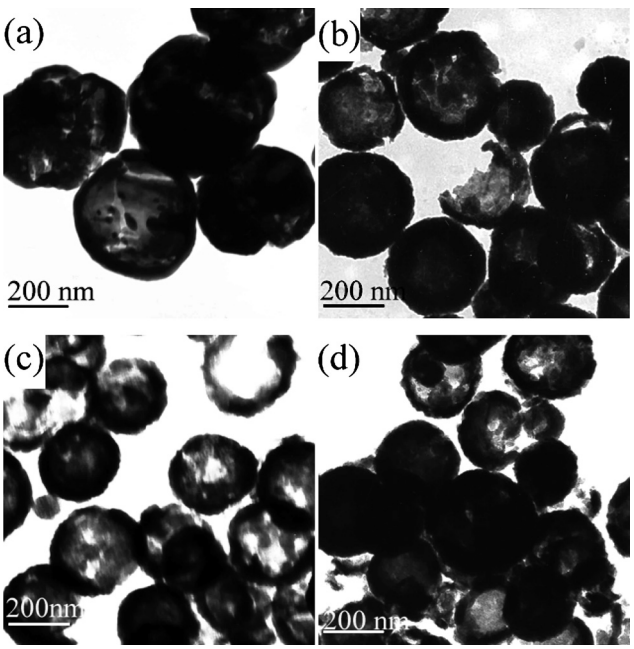

Fig. 4 TEM images of EuF_3 hollow sub-microspheres with diameters of *ca* (a) 410–450 nm, (b) 350–400 nm, (c) 300–330 nm and (d) 280–320 nm, which were obtained in 0.125, 0.133, 0.143, and 0.154 M $Eu(NO_3)_3$ solution at 110 °C for 8 h, respectively.

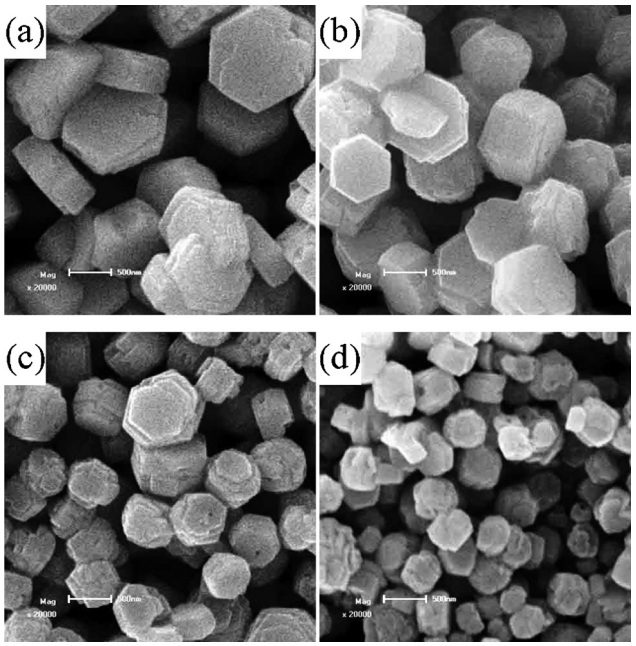

Fig. 5 SEM images of EuF_3 hexagonal microdisc crystals with diameters of *ca* (a) 1100–1200 nm, (b) 700–1000 nm, (c) 500–850 nm and (d) 400–550 nm, which were obtained in 0.200, 0.182, 0.154 and 0.143 M $Eu(NO_3)_3$ solution at 110 °C for 14 h, respectively.

In order to evaluate the influence of oleic acid and EDTA on the morphology of the product, we prepared a series of products in 0.2 M $Eu(NO_3)_3$ solution when simply removing EDTA or/and oleic acid from the synthetic system. The morphologies of the products were characterized by TEM. When the system did not contain any EDTA, the final products were irregular particles (Fig. 6a). When oleic acid was removed from the synthesis systems, the resultant products were a mixture of spherical aggregates and hollow microspheres with diameters of *ca* 100–250 nm (Fig. 6b). Moreover, the reaction time hardly affected the morphology of the product obtained in such conditions. Prolonging the reaction time to 16 h or longer has no obvious change on the morphology of the products, and no microdisc crystal could be observed. When neither EDTA nor oleic acid was employed, the as-prepared products presented irregular shapes (Fig. 6c).

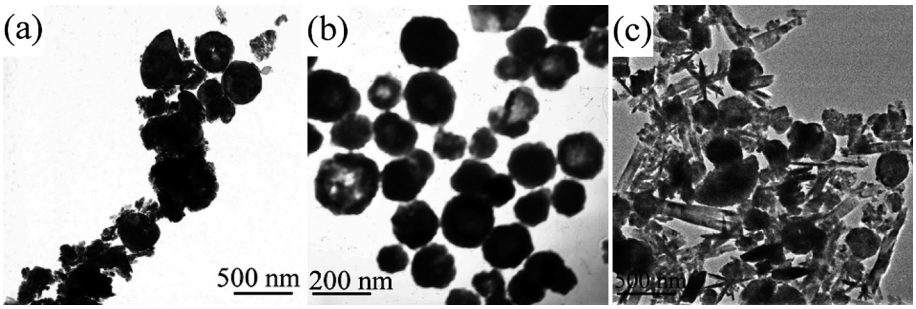

Fig. 6 TEM images of the EuF_3 prepared in 0.2 M $Eu(NO_3)_3$ solution: (a) without EDTA, (b) without oleic acid and (c) without EDTA and oleic acid.

To investigate the formation mechanism of EuF_3 hollow sub-microspheres and hexagonal microdisc crystals, we studied the effect of reaction time on the morphology of products. Fig. 7 is a series of TEM images of the samples showing morphological evolution of the hollow sub-microspheres and hexagonal microdiscs. When the sample was prepared without heat treatment, only primary particles are observed, as shown in Fig. 7a. The corresponding XRD pattern (Fig. 3d) indicates that the primary particles without hydrothermal treatment did not lead to any detectable crystalline phase. After 2 h hydrothermal treatment, spherical aggregates with diameters of *ca* 250–360 nm were formed. TEM image indicates that these aggregates were solid and no hollow structure was found (Fig. 7b). The XRD result shows that the spherical aggregates were a pure hexagonal EuF_3 phase (Fig. 3c). Extending the thermally treating time to 6–8 h resulted in distinct changes in particle morphology. In the typical TEM image of the products *via* 6 h of hydrothermal treatment, hollow spheres with diameters of *ca* 250–320 nm can be easily seen (Fig. 7c). The solid evacuation is much more pronounced after 8 h of reactive aging. It is found that during the hollowing process the size of these sub-microspheres does not change much. The hollow sub-microspheres can convert to hexagonal microdisc crystals gradually when the reaction time is longer than 8 h. When prolonging the reaction time to 9–12 h, the product was found to be a mixture of hollow sub-microspheres and hexagonal microdisc crystals (Fig. 7d and 7e). The evacuation of spherical aggregates is much more pronounced after 14 h of reactive aging (Fig. 7f). The formed microdisc crystals are quite uniform with a 100% morphological yield. Moreover, the intensities of the diffraction peaks of EuF_3 microdiscs increase significantly (Fig. 3a).

The formation mechanism of EuF_3 hollow sub-microspheres and hexagonal microdisc crystals can now be further addressed. As depicted in Scheme 1, the sphere formation and related

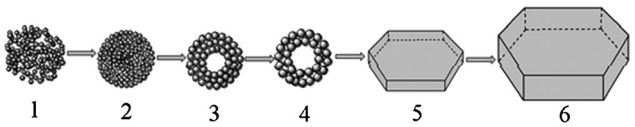

Scheme 1 Formation process of EuF_3 hollow sub-microspheres and hexagonal microdisc crystals: aggregation of nanocrystallites into solid spheres (1 and 2); creation of a hollow interior *via* Ostwald ripening (3 and 4) and construction of microdisc crystals by an oriented attachment mechanism (5 and 6).

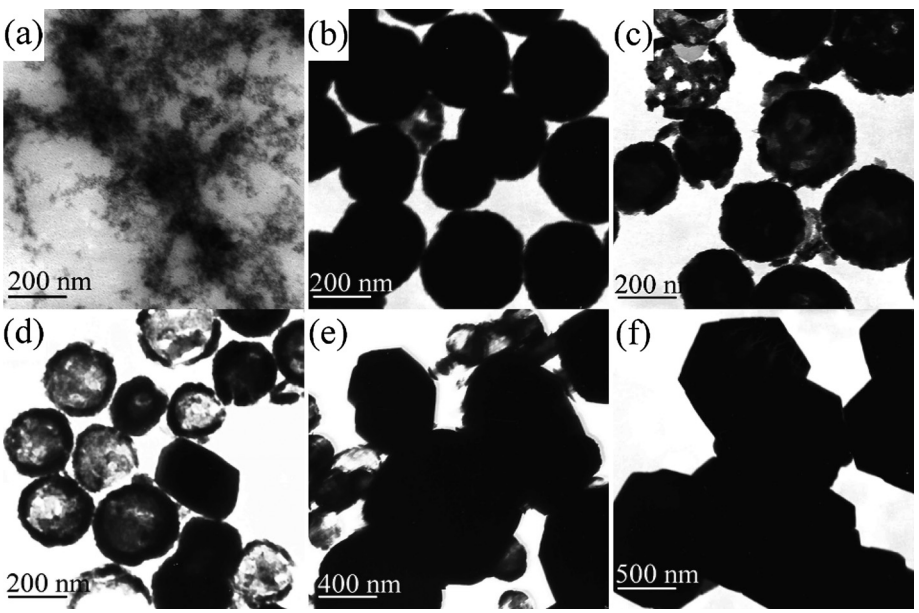

Fig. 7 TEM images of EuF_3 samples obtained in 0.2 M $Eu(NO_3)_3$ solution (a) without hydrothermal treatment; (b–f) at 110 °C for 2, 6, 9, 12 and 14 h, respectively.

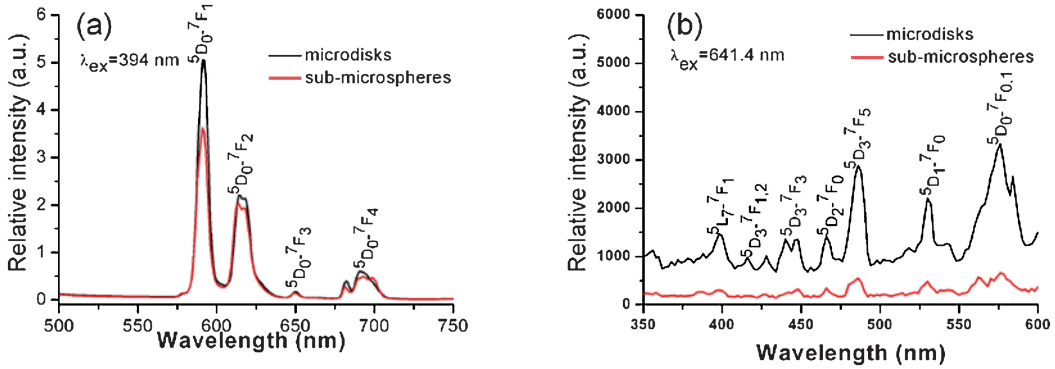

Fig. 8 (a) Down-conversion and (b) up-conversion spectra of EuF_3 hollow sub-microspheres and hexagonal microdisc crystals obtained in 0.2 M $Eu(NO_3)_3$ solution. (λ_{ex} = 394 nm for down-conversion, λ_{ex} = 641.4 nm for up-conversion).

hollowing can be explained by a self-transformation process within the same aggregated particles accompanied by the localized Ostwald ripening (1–4), while the formation of a hexagonal microdisc crystal can be ascribed to an oriented attachment mechanism (5–6). In other words, the primary EuF_3 particles were synthesized and aggregated together to form spherical aggregates. At this stage, these aggregated EuF_3 microspheres are not in a thermodynamically equilibrium status and would redistribute matter from the interior to the exterior of the aggregates by a localized Ostwald ripening, resulting in the formation of EuF_3 nanocrystals composing the sub-microspheres with a hollow interior. With the reaction continuing, the nanocrystals of the sub-microspheres aggregated around some cores to form hexagonal discs through oriented attachment. Then, the adjacent nanocrystals would fuse into the core section to form bigger single-crystalline discs. These hexagonal discs would further attract the nanocrystals to attach on their surface and repeat the fusion process to grow bigger until the microspheres were consumed. In our experiment, the surfactants play an important role in the process. The oleic acid serves as a diffusion boundary to restrain rapid crystal growth and prevent direct fusion among the small particles during the initial stage. Subsequently, these primary particles can be mediated by the adsorbed ligands on the crystal surface and serve as seeds for the growth of highly anisotropic nanostructures in the oriented attachment mechanism. According to the Bravais–Friedel–Donnay–Harker (BFDH) law[37] and the Hartman–Perdok approach,[38] the as-grown crystal morphology is dominated by the slow-growing faces because the fast-growing faces may grow out and not be represented in the final crystal habit. In our synthesis systems, EDTA may act as capped reagents and be adsorbed on the {0001} facets, further decreasing the surface energy of these facets, and consequently prohibiting the radial enlargement in the [0001] direction and driving the growth of nuclei along six symmetric directions of $\{10\bar{1}0\}$. It is noteworthy that the sub-microspheres were completely consumed by 14 h of hydrothermal treatment, and no hexagonal microdisc crystals were obtained within 8 h of reaction aging. So it is reasonable to suggest that coarsening by a conventional Ostwald ripening mechanism of dissolution and growth of primary particles would first occur before the starting of oriented attachment, which is similar to the formation of single crystalline $PbMoO_4$ dendrites.[39]

Up- and down-conversion emissions were recorded on the solid samples of EuF_3 nanostructures at room temperature (Fig. 8). At the excited wavelength of 394 nm, the corresponding emission peaks of the products at 591, 614, 650, 681–693 nm were observed, corresponding to the $^5D_0$–$^7F_1$, $^5D_0$–$^7F_2$, $^5D_0$–$^7F_3$ and $^5D_0$–$^7F_4$ transitions in Eu^{3+}, respectively.[40] When the species were excited at 641.4 nm, the emission peaks at 398, 416, 427.5, 440–447, 466, 486, 530, 576 and 583 nm were observed, which are assigned to $^5L_7$–$^7F_1$, $^5D_3$–$^7F_1$, $^5D_3$–$^7F_2$, $^5D_3$–$^7F_3$, $^5D_2$–$^7F_0$, $^5D_3$–$^7F_5$, $^5D_1$–$^7F_0$, $^5D_0$–$^7F_0$ and $^5D_0$–$^7F_1$ transitions of Eu^{3+},[41,42] respectively. Although the emission positions of these samples are identical, the emission intensity of hexagonal microdisc crystals is higher than that of the sub-microspheres under the same measurement conditions. It is generally believed that morphology and crystallinity should influence the luminescent properties of nanostructured particles. XRD results show that the crystal intensity of hexagonal microdisc crystals and sub-microspheres is different. Therefore, the difference in luminescent properties may be ascribed to the various morphologies and degrees of crystallinity.

Conclusions

In summary, we have presented a facile and mild hydrothermal route to the synthesis of hollow sub-microspheres and hexagonal microdisc crystals. The formation and evolution of EuF_3 structures were investigated, and the Ostwald ripening and oriented attachment mechanisms clearly contribute to the formation of hollow sub-microspheres and hexagonal microdisc crystals, respectively. Moreover, the Ostwald ripening mechanism acted to form the secondary particles before oriented attachment. This crystal growth mode may give us a new insight into the growth of EuF_3 hexagonal microdisc crystals and opens a new way for controlled synthesis of other well-defined crystals in morphology and dimensionality.

Experimental

All chemicals and reagents were analytical grade, purchased from Sinopharm Chemical Reagent Co., Ltd. (Shanghai, China), and used without further purification. Deionized water was used throughout. In a typical synthesis, EDTA solution was obtained by dissolving 500 mg EDTA in 6.5 ml of 1 M ammonium

solution. Subsequently, 200 mg NH_4F and 5 ml ethanol were added into the EDTA solution to get solution A. 1 mmol Eu_2O_3 was completely dissolved in 5 ml of 1 M HNO_3 to form $Eu(NO)_3$ solution. 0–3 ml water was added to the $Eu(NO)_3$ solution to get 0.125–0.2 M $Eu(NO)_3$ solution. Then, 2 ml of 1 M ammonia solution, 5 ml ethanol and 5 ml oleic acid were added to the obtained $Eu(NO)_3$ solution in sequence. After 5 min of ultrasonic bath, solution A was introduced. Subsequently, the mixed system was sonolyzed for 5 min to ensure homogeneous dispersion of all reagents in the solutions and was transferred into a Teflon-lined autoclave. After the autoclave was tightly sealed and heated at 110 °C for 0–14 h, the system was allowed to cool to room temperature naturally. The as-obtained white precipitate was collected, washed with distilled water and absolute ethanol several times, and finally dried at 110 °C in air for 1 h.

XRD patterns of the products were recorded on a Shimadzu XRD-6000 X-ray diffractometer with Cu Ka radiation (λ = 0.15406 nm) at a scanning rate of 0.1° s^{-1} in the 2θ range from 20 to 80°. TEM images were obtained on a JEM-200CX transmission electron microscope, with an accelerating voltage of 200 kV. SEM images were acquired from a Shimadzu SSX-550 scanning electron microscope. HRTEM images were taken on a FEI Tecnai G2 S-Twin instrument with a field emission gun operating at 300 kV. Down-conversion luminescent spectra were performed on an Aminco Bowman luminescence spectrometer. Up-conversion luminescent spectra were carried out on an Edinburgh Instrument FLS 920 combined fluorescence lifetime and steady state spectrometer. The excitation source was a coherent two-pin 641.4 nm semiconductor diode laser with a maximum power of 5 mW. A 100 μm core fiber was coupled to the diode laser. A red-sensitive Peltier-cooled Hamamatsu R955 photomultiplier tube (PMT), with a photoncounting interface, was used for analyses between λ = 350–600 nm.

Acknowledgements

This work is supported by the National Natural Science Foundation of P. R. China. (20535020, 20671051, 20721002 and 90813020) and the National Basic Research Program of P. R. of China (2007CB925102).

References

1 S. H. Im, Y. T. Lee, B. Wiely and Y. N. Xia, *Angew. Chem., Int. Ed.*, 2005, **44**, 2154.
2 V. F. Puntes, K. M. Krishnan and A. P. Alivisatos, *Science*, 2001, **291**, 2115.
3 Y. N. Xia, P. D. Yang, Y. G. Sun, Y. Y. Wu, B. Mayers, B. Gates, Y. D. Yin, F. Kim and H. Q. Yan, *Adv. Mater.*, 2003, **15**, 353.
4 F. C. Cheng, J. Z. Zhao, C. S. Li, H. Ma, J. Chen and P. W. Shen, *Inorg. Chem.*, 2006, **45**, 2038.
5 J. Li and H. C. Zeng, *J. Am. Chem. Soc.*, 2007, **129**, 15839.
6 Y. X. Zhang and H. C. Zeng, *Langmuir*, 2008, **24**, 3740.
7 H. C. Zeng, *Curr. Nanosci.*, 2007, **3**, 177.
8 H. G. Yang and H. C. Zeng, *J. Phys. Chem. B*, 2004, **108**, 3492.
9 H. C. Zeng, *J. Mater. Chem.*, 2006, **16**, 649.
10 Y. Chang, J. J. Teo and H. C. Zeng, *Langmuir*, 2005, **21**, 1074.
11 Y. X. Zhang, G. H. Li, Y. C. Wu, Y. Y. Luo and L. D. Zhang, *J. Phys. Chem. B*, 2005, **109**, 5478.
12 B. Liu and H. C. Zeng, *Small*, 2005, **1**, 566.
13 J. Li and H. C. Zeng, *Angew. Chem., Int. Ed.*, 2005, **44**, 4342.
14 J. J. Teo, Y. Chang and H. C. Zeng, *Langmuir*, 2006, **22**, 7369.
15 X. W. Lou, Y. Wang, C. L. Yuan, J. Y. Lee and L. A. Archer, *Adv. Mater.*, 2006, **18**, 2325.
16 J. G. Yu, H. T. Guo, S. A. Davis and S. Mann, *Adv. Funct. Mater.*, 2006, **16**, 2035.
17 H. G. Yu, J. G. Yu, S. W. Liu and S. Mann, *Chem. Mater.*, 2007, **19**, 4327.
18 C. T. Campbell, S. C. Parker and D. E. Starr, *Science*, 2002, **298**, 811.
19 F. Huang, H. Z. Zhang and J. F. Banfield, *Nano Lett.*, 2003, **3**, 373.
20 J. Zhang, Z. Lin, Y. Z. Lan, G. Q. Ren, D. G. Chen, F. Huang and M. C. Hong, *J. Am. Chem. Soc.*, 2006, **128**, 12981.
21 H. C. Zeng, *Int. J. Nanotechnol.*, 2007, **4**, 329.
22 J. W. Stouwdam and F. C. J. M. van Veggel, *Nano Lett.*, 2002, **2**, 733.
23 G. S. Yi, H. C. Lu, S. Y. Zhao, G. Yue, W. J. Yang, D. P. Chen and L. H. Guo, *Nano Lett.*, 2004, **4**, 2191.
24 L. Y. Wang and Y. D. Li, *Chem. Commun.*, 2006, 2557.
25 H. Schäfer, P. Ptacek, K. Kömpe and M. Haase, *Chem. Mater.*, 2007, **19**, 1396.
26 R. X. Yan and Y. D. Li, *Adv. Funct. Mater.*, 2005, **15**, 763.
27 X. Wang and Y. D. Li, *Angew. Chem., Int. Ed.*, 2003, **42**, 3497.
28 X. Wang and Y. D. Li, *Chem.–Eur. J.*, 2003, **9**, 5627.
29 X. Wang, J. Zhuang, Q. Peng and Y. D. Li, *Inorg. Chem.*, 2006, **45**, 6661.
30 J. L. Lemyre and A. M. Ritcey, *Chem. Mater.*, 2005, **17**, 3040.
31 G. Y. Li, Y. H. Ni, J. M. Hong and K. M. Liao, *CrystEngComm*, 2008, **10**, 1681.
32 L. Ma, W. X. Chen, Y. F. Zheng, J. Zhao and Z. D. Xu, *Mater. Lett.*, 2007, **61**, 2765.
33 Y. W. Zhang, X. Sun, R. Si, L. P. You and C. H. Yan, *J. Am. Chem. Soc.*, 2005, **127**, 3260.
34 L. Zhu, X. M. Liu, J. Meng and X. Q. Cao, *Cryst. Growth Des.*, 2007, **7**, 2505.
35 M. Wang, Q. L. Huang, J. M. Hong, X. T. Chen and Z. L. Xue, *Cryst. Growth Des.*, 2006, **6**, 2169.
36 M. Wang, Q. L. Huang, J. M. Hong, X. T. Chen and Z. L. Xue, *Cryst. Growth Des.*, 2006, **6**, 1972.
37 D. Winn and M. F. Doherty, *AICHE J.*, 2000, **46**, 1348.
38 P. Hartman and W. G. Perdok, *Acta Crystallogr.*, 1955, **8**, 49–52, 521–524, 525–529.
39 Y. Cheng, Y. S. Wang, D. Q. Chen and F. Bao, *J. Phys. Chem. B*, 2005, **109**, 794.
40 M. Flores-Acosta, R. Pérez-Salas, R. Aceves, M. Sotelo-Lerma and R. Ramírez-Bon, *Solid State Commun.*, 2005, **136**, 567.
41 L. G. Deshazer and G. H. Dieke, *J. Chem. Phys.*, 1963, **38**, 2190.
42 C. X. Li, Z. W. Quan, J. Yang, P. P. Yang and J. Lin, *Inorg. Chem.*, 2007, **46**, 6329.

